A Unity Power Factor PWM Rectifier with DC Ripple Compensation

Toshihisa Shimizu, *Member, IEEE,* Tsutomu Fujita, Gunji Kimura, *Member, IEEE,* and Jun Hirose

***Abstract*—This paper presents a new topology for a pulsewidth modulation (PWM) rectifier which achieves unity power factor on the ac supply side and ripple reduction on the dc output side. The main circuit of this rectifier consists of a conventional PWM rectifier and a pair of additional switches. The switches and PWM rectifier are controlled such that the ripple current on the dc line is reduced, and unity power factor is achieved on the ac line. As a result, this circuit does not require a large dc capacitor or a passive *LC* resonant circuit. Furthermore, control of the additional switches and PWM rectifier requires only a simple control circuit. The effectiveness of this circuit was confirmed by experiments and analysis. The rectifier is useful for uninterruptible power systems (UPS's) and dc power supplies, especially for cases in which batteries are connected to the dc line.**

***Index Terms*—Battery, PWM converter, ripple.**

I. Introduction

THE GENERATION of harmonics and their subsequent propagation into utility lines is a topic of increasing concern for power providers. To reduce harmonics on power lines, unity power factor pulsewidth modulation (PWM) rectifiers are used to supply input power to an ac–dc power conversion plant. However, these single-phase PWM rectifiers have serious defects. For example, low-frequency ripple current increases in proportion to the input current to the ac-dc plant and appears as low-frequency ripple voltage on the dc line. It is usually necessary to connect a very large capacitor or a passive *LC* filter circuit to the dc line in order to reduce the low-frequency ripple voltage, as shown in Fig. 1 [1], [2]. When batteries are connected to the dc output, most of the dc ripple current generated by the PWM rectifier flows into the battery, because the impedance of the battery is very low compared to that of the prior-art circuit. Battery ripple current, especially at low frequencies, results in battery heating and a corresponding rise in temperature. It is well known that battery lifetime decreases as temperature increases.

In this paper, a new topology for PWM rectification which reduces the low-frequency battery ripple current is presented. This new topology is accomplished by simply adding a pair of switching devices to a conventional PWM rectifier circuit. Using a simple control technique, the ripple energy on the dc line is converted through the action of the additional switches into energy, which is stored in the input capacitors. The ripple-reducing effect of this rectifier is confirmed by experiments using a breadboard setup.

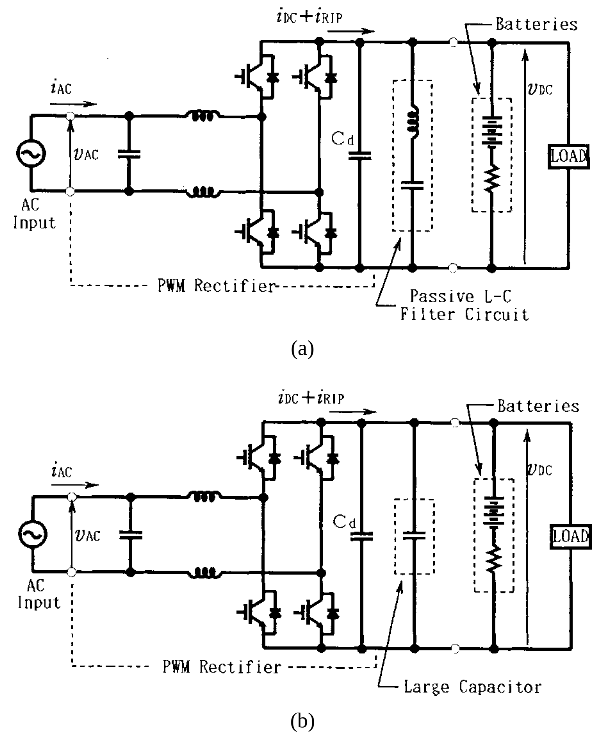

Fig. 1. Conventional PWM rectifier topologies.

II. Circuit Configuration

Fig. 2 shows the configuration of the main circuit of the proposed PWM rectifier. The conventional portion of the PWM rectifier consists of the U-phase switches $(S1, S2)$, V-phase switches $(S3, S4)$, a dc capacitor (Cd), input ac filter inductors $(L1, L2)$, resistive components for the ac filters $(r1, r2)$, and input ac filter capacitors $(C1, C2)$. The additional switches $(S5, S6)$, which we call Z-phase switches, are connected to two terminals on the dc output line, and the junction of $S5$ and $S6$ is connected to the junction of capacitors $C1$ and $C2$. The switching frequency of switches $S1$–$S6$ is set very high compared to the ac input frequency. Parameters of the main circuit components are selected to provide fast response time, in order to control the ac inductor currents. Under the proposed dc ripple-reduction control, the current flowing through the dc capacitor Cd contains only the

Manuscript received November 18, 1995; revised November 17, 1996.
T. Shimizu and G. Kimura are with the Faculty of Technology, Tokyo Metropolitan University, Tokyo, 192-03 Japan.
T. Fujita was with Tokyo Metropolitan University, Tokyo, 192-03 Japan. He is now with the East Japan Railway Company, Ltd., Tokyo, 114 Japan.
J. Hirose is with Fuji Electric Company, Ltd., Tokyo, 191 Japan.
Publisher Item Identifier S 0278-0046(97)05261-1.

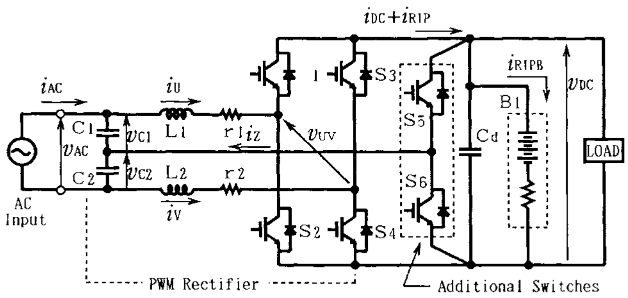

Fig. 2. Main circuit of proposed PWM rectifier.

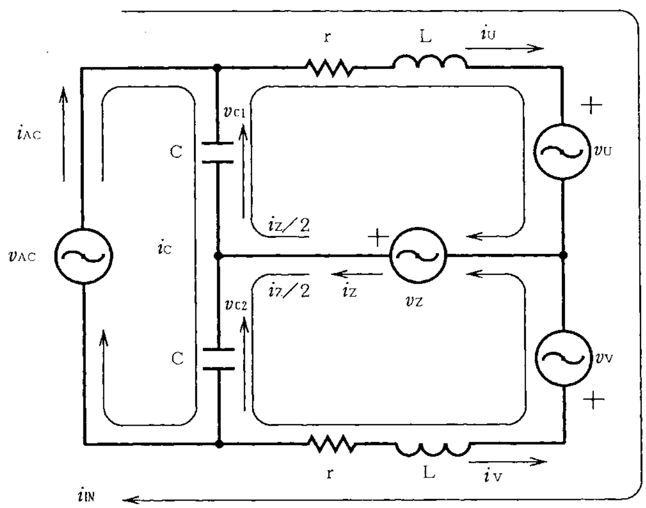

Fig. 3. Equivalent circuit of proposed PWM rectifier.

high-frequency component resulting from the high-frequency switching. Thus, the capacitance of Cd can be made very low. Using a smaller capacitor helps to reduce the size of the entire PWM system.

III. Principles of Operation

Fig. 3 shows the equivalent circuit of the proposed rectifier. The following assumptions are made.

1) Because the switching frequency is very high, almost all of the ripple current caused by the switching flows into the dc capacitor, and very little flows into the battery. Only the low-frequency ripple current, caused by the rectification of input ac current, flows into the battery.
2) The losses in the switching devices are negligible.
3) AC capacitors $C1$ and $C2$ have the same capacitance $C; C = C1 = C2$.
4) Inductors $L1$ and $L2$ have the same inductance L; $L = L1 = L2$.
5) Resistors $r1$ and $r2$ have the same resistance $r; r = r1 = r2$.

Each pair of rectifier arms ($S1$ and $S2, S3$ and $S4, S5$ and $S6$) are defined as independent ac voltage sources, v_U, v_V, and v_Z, respectively. Since the U-phase and V-phase switches are controlled symmetrically, v_U and v_V are related as follows:

$$v_U = -v_V. \tag{1}$$

In our case, the Z-phase current i_Z, which flows from the voltage source v_Z is divided equally into U-phase and V-phase current (i_U and i_V) with an amplitude of $i_Z/2$. Therefore, the reactor currents i_U and i_V and the ac input current i_{ac} are

$$i_U = i_Z/2 + i_{\text{IN}} \tag{2}$$
$$i_V = i_Z/2 - i_{\text{IN}} \tag{3}$$

and

$$i_{\text{ac}} = i_C + i_{\text{IN}}. \tag{4}$$

Then, we can define the current i_{IN} to be

$$i_{\text{IN}} = (i_U - i_V)/2. \tag{5}$$

Equation (5) shows that we can obtain a sinusoidal input current by controlling the current i_{IN} without influencing the Z-phase current.

Next, we define the voltages on the ac capacitors $C1$ and $C2$ and input ac voltage as v_{C1}, v_{C2}, and v_{ac}, respectively. From Fig. 3, we obtain the following:

$$v_{\text{ac}} = v_{C1} + v_{C2} \tag{6}$$
$$v_{C1} = v_U - v_Z + i_U \cdot r + L \cdot di_U/dt \tag{7}$$

and

$$v_{C2} = -v_V + v_Z - i_V \cdot r + L \cdot di_V/dt. \tag{8}$$

The low-frequency voltage components across inductors $L1$ and $L2$ and resistors $r1$ and $r2$ are usually small compared to the other low-frequency voltage components, such as $v_{\text{ac}}, v_{C1}, v_{C2}, v_U, v_V$, and v_Z, although the losses on the resistors $r1$ and $r2$ cannot be neglected. Therefore, (7) and (8) can be simplified as follows:

$$v_{C1} \cong v_U - v_Z \tag{9}$$

and

$$v_{C2} \cong -v_V + v_Z. \tag{10}$$

From (1), (9), and (10), the sum P_c of the low-frequency generated energy stored in the ac capacitors $C1$ and $C2$ is, at any instant,

$$\begin{aligned} P_c &\cong C(v_U - v_Z)^2/2 + C(-v_V + v_Z)^2/2 \\ &= C(v_U - v_Z)^2. \end{aligned} \tag{11}$$

In (11), v_U is used to control the input current i_{IN}, but v_Z is independent of that control. Therefore, P_c can be controlled by controlling v_Z. It should be noted that the energy Pc is obtained from the output dc line by controlling the Z-phase switch. Hence, if v_Z is controlled appropriately, the energy appearing on the dc line is converted to P_c.

As a result, this circuit achieves not only input unity power factor with the sinusoidal input current, but also reduction of the dc ripple current.

IV. Theoretical Analysis

To obtain the transfer function of this circuit, a state-space averaging technique [5] was used. For the first step of the analysis, the equivalent circuit for each stage of operation was determined as shown in Fig. 4. The dc output voltage

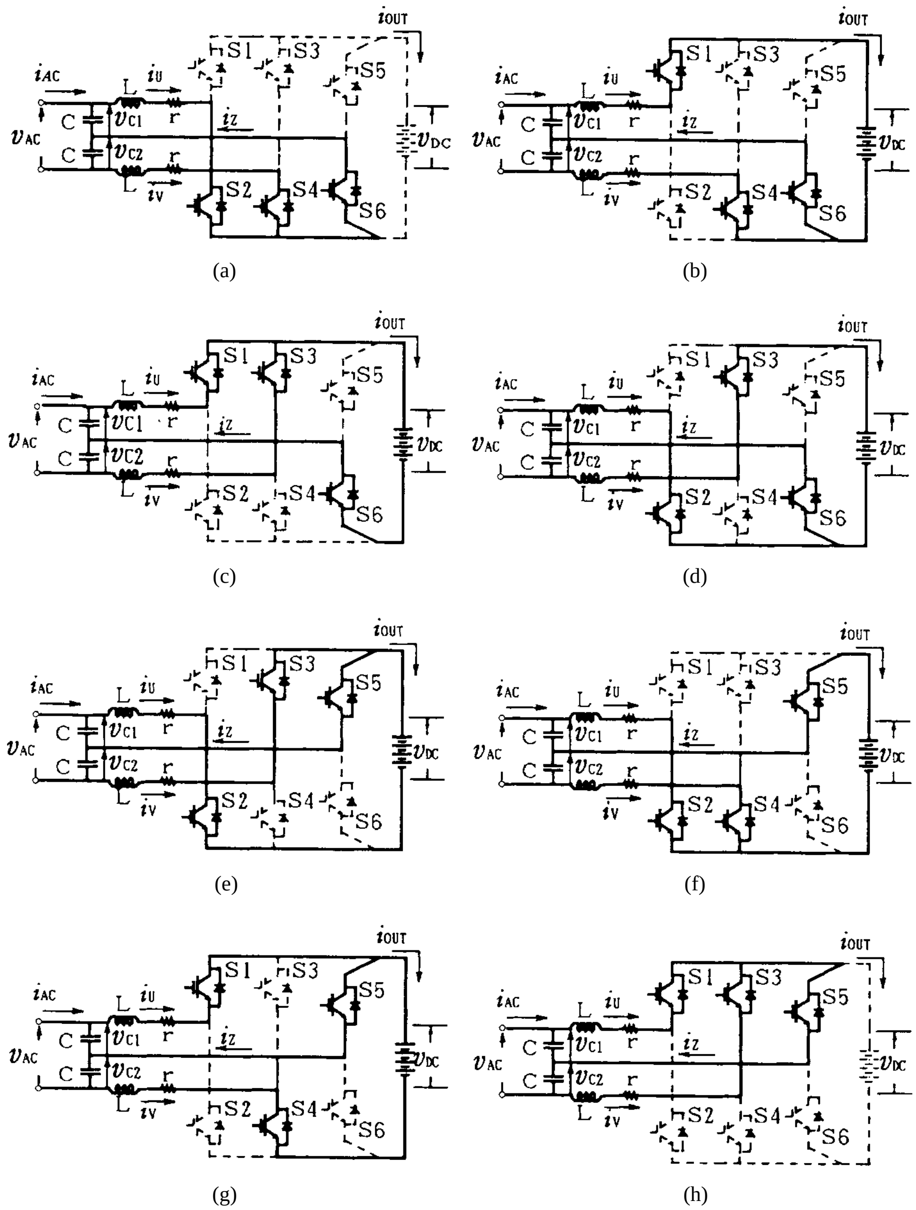

Fig. 4. Equivalent circuit of proposed PWM rectifier for each stage of operation. (a) Stage 1. (b) Stage 2. (c) Stage 3. (d) Stage 4. (e) Stage 5. (f) Stage 6. (g) Stage 7. (h) Stage 8.

$v_{\rm dc}$ was considered to be constant. In each equivalent circuit, state equations were introduced. For the first stage, shown in Fig. 4(a), the equations are as follows:

$$v_{C1} = L\frac{di_U}{dt} + r \cdot i_U \tag{12}$$

$$v_{C2} = -L\frac{di_V}{dt} - r \cdot i_V \tag{13}$$

$$i_{\rm ac} = C\frac{dv_{C1}}{dt} + i_U = \frac{dv_{C2}}{dt} - i_V \tag{14}$$

and

$$\alpha = \frac{dv_{\rm ac}}{dt}. \tag{15}$$

Then, the state equation for Stage 1 [Fig. 4(a)] is

$$\frac{d\boldsymbol{X}}{dt} = \boldsymbol{AX} + \boldsymbol{B}_1\boldsymbol{V} \tag{16}$$

where the state variables $\boldsymbol{X}$ and $\boldsymbol{V}$ and matrices $\boldsymbol{A}$ and $\boldsymbol{B}_1$ are

$$\boldsymbol{X} = [i_U \quad i_V \quad v_{C1}]^T, \qquad \boldsymbol{V} = [v_{\rm dc} \quad v_{\rm ac} \quad \alpha]^T$$

$$\alpha = \frac{dv_{\rm ac}}{dt}$$

$$\boldsymbol{A} = \begin{bmatrix} -r/L & 0 & 1/L \\ 0 & -r/L & 1/L \\ -1/(2C) & -1/(2C) & 0 \end{bmatrix}$$

$$\boldsymbol{B}_1 = \begin{bmatrix} 0 & 0 & 0 \\ 0 & -1/L & 0 \\ 0 & 0 & 1/2 \end{bmatrix}.$$

We can derive state equations for each stage, making it is possible to define matrix $\boldsymbol{A}$ as a common matrix. Matrix $\boldsymbol{B}_n$ $(n$

refers to the stage number shown in Fig. 4) varies as follows:

$$\boldsymbol{B}_1 = \begin{pmatrix} 0 & 0 & 0 \\ 0 & -1/L & 0 \\ 0 & 0 & 1/2 \end{pmatrix}$$
$$\boldsymbol{B}_2 = \begin{pmatrix} -1/L & 0 & 0 \\ 0 & -1/L & 0 \\ 0 & 0 & 1/2 \end{pmatrix}$$
$$\boldsymbol{B}_3 = \begin{pmatrix} -1/L & 0 & 0 \\ -1/L & -1/L & 0 \\ 0 & 0 & 1/2 \end{pmatrix}$$
$$\boldsymbol{B}_4 = \begin{pmatrix} 0 & 0 & 0 \\ -1/L & -1/L & 0 \\ 0 & 0 & 1/2 \end{pmatrix}$$
$$\boldsymbol{B}_5 = \begin{pmatrix} 1/L & 0 & 0 \\ 0 & -1/L & 0 \\ 0 & 0 & 1/2 \end{pmatrix}$$
$$\boldsymbol{B}_6 = \begin{pmatrix} 1/L & 0 & 0 \\ 1/L & -1/L & 0 \\ 0 & 0 & 1/2 \end{pmatrix}$$
$$\boldsymbol{B}_7 = \begin{pmatrix} 0 & 0 & 0 \\ 1/L & -1/L & 0 \\ 0 & 0 & 1/2 \end{pmatrix}$$
$$\boldsymbol{B}_8 = \begin{pmatrix} 0 & 0 & 0 \\ 0 & -1/L & 0 \\ 0 & 0 & 1/2 \end{pmatrix}.$$

In conventional single-phase PWM inverters, the switches in the two legs of the inverter circuit are switched according to the unipolar voltage switching scheme, in which there are four combinations of switch ON states (see [5], Figs. 6–15). In our switching scheme, shown in Fig. 6, legs U, V, and Z of the rectifier are controlled by comparing the modulation signal $e\mathrm{tri}$ with the U-phase signal e_U, V-phase signal e_V, and Z-phase signal e_Z, respectively. Therefore, the modulation signal level has six states which lead to the switching patterns shown in Fig. 5. In each pattern, the switches of each leg are triggered ON according to the following conditions:

$$e_U > e\mathrm{tri}\text{: } S1 \text{ is ON;} \quad e_U < e\mathrm{tri}\text{: } S2 \text{ is ON}$$
$$e_V > e\mathrm{tri}\text{: } S3 \text{ is ON;} \quad e_V < e\mathrm{tri}\text{: } S4 \text{ is ON}$$
$$e_Z > e\mathrm{tri}\text{: } S5 \text{ is ON;} \quad e_Z < e\mathrm{tri}\text{: } S6 \text{ is ON.}$$

Furthermore, if the frequency f_S of the modulation signal $e\mathrm{tri}$ is kept constant, the switching period $(T_S = 1/f_S)$ of each switch is constant, and the ON period of each switch is as shown in Fig. 5. Therefore, duty ratios D_U, D_V, and D_Z of switches $S1, S3$, and $S5$, respectively, are defined as follows:

$$D_U = D_U \cdot T_S/T_S\text{: ON Duty Ratio of } S1;$$
$$D_V = D_V \cdot T_S/T_S\text{: ON Duty Ratio of } S3;$$
$$D_Z = D_Z \cdot T_S/T_S\text{: ON Duty Ratio of } S5.$$

Furthermore, because switches $S1$ and $S2, S3$ and $S4, S5$ and $S6$ are triggered ON/OFF alternately, the duty ratios of $S2, S4$, and $S6$ are

$$1 - D_U = (T_S - D_U \cdot T_S)/T_S\text{: ON Duty Ratio of } S2;$$
$$1 - D_V = (T_S - D_V \cdot T_S)/T_S\text{: ON Duty Ratio of } S4;$$
$$1 - D_Z = (T_S - D_Z \cdot T_S)/T_S\text{: ON Duty Ratio of } S6.$$

It should be noted that each of the switching patterns (a)–(f), which correspond to Fig. 5(a)–(f), includes four stages from among stages (1)–(8) shown in Fig. 4. For example, switching pattern (a) includes stages (1), (6), (5), and (8) of Fig. 4. Using the duty ratios and the state equations, we obtain the averaged state equation for switching patterns (a)–(f):

switching pattern (a):

$$\frac{d\overline{\boldsymbol{X}}}{dt} = \boldsymbol{A}\overline{\boldsymbol{X}} + ((1 - D_Z)\boldsymbol{B}_1 + (D_Z - D_U)\boldsymbol{B}_6 + (D_U - D_V)\boldsymbol{B}_7 + D_V\boldsymbol{B}_8)\boldsymbol{V} \tag{17}$$

switching pattern (b):

$$\frac{d\overline{\boldsymbol{X}}}{dt} = \boldsymbol{A}\overline{\boldsymbol{X}} + ((1 - D_U)\boldsymbol{B}_1 + (D_U - D_Z)\boldsymbol{B}_2 + (D_Z - D_V)\boldsymbol{B}_7 + D_V\boldsymbol{B}_8)\boldsymbol{V} \tag{18}$$

switching pattern (c):

$$\frac{d\overline{\boldsymbol{X}}}{dt} = \boldsymbol{A}\overline{\boldsymbol{X}} + ((1 - D_U)\boldsymbol{B}_1 + (D_U - D_V)\boldsymbol{B}_2 + (D_V - D_Z)\boldsymbol{B}_3 + D_Z\boldsymbol{B}_8)\boldsymbol{V} \tag{19}$$

switching pattern (d):

$$\frac{d\overline{\boldsymbol{X}}}{dt} = \boldsymbol{A}\overline{\boldsymbol{X}} + ((1 - D_Z)\boldsymbol{B}_1 + (D_Z - D_V)\boldsymbol{B}_6 + (D_V - D_U)\boldsymbol{B}_5 + D_U\boldsymbol{B}_8)\boldsymbol{V} \tag{20}$$

switching pattern (e):

$$\frac{d\overline{\boldsymbol{X}}}{dt} = \boldsymbol{A}\overline{\boldsymbol{X}} + ((1 - D_V)\boldsymbol{B}_1 + (D_V - D_Z)\boldsymbol{B}_4 + (D_z - D_U)\boldsymbol{B}_5 + D_U\boldsymbol{B}_8)\boldsymbol{V} \tag{21}$$

switching pattern (f):

$$\frac{d\overline{\boldsymbol{X}}}{dt} = \boldsymbol{A}\overline{\boldsymbol{X}} + (1 - D_V)\boldsymbol{B}_1 + (D_V - D_U)\boldsymbol{B}_4 + (D_U - D_Z)\boldsymbol{B}_3 + D_Z\boldsymbol{B}_8)\boldsymbol{V}. \tag{22}$$

By substituting $\boldsymbol{B}_1$–$\boldsymbol{B}_8$ into (17)–(22), we obtain the pattern-independent averaged state equation:

$$\frac{d\overline{\boldsymbol{X}}}{dt} = \boldsymbol{A}\overline{\boldsymbol{X}} + \boldsymbol{B}\boldsymbol{V} \tag{23}$$

where the state space averaging vector $\boldsymbol{B}$ and state-space variable $\overline{\boldsymbol{X}}$ are

$$\boldsymbol{B} = \begin{pmatrix} (D_Z - D_U)/L & 0 & 0 \\ (D_V - D_Z)/L & -1/L & 0 \\ 0 & 0 & 1/2 \end{pmatrix}$$
$$\overline{\boldsymbol{X}} = [\bar{i}_U \quad \bar{i}_V \quad \overline{v}_{C1}]^T.$$

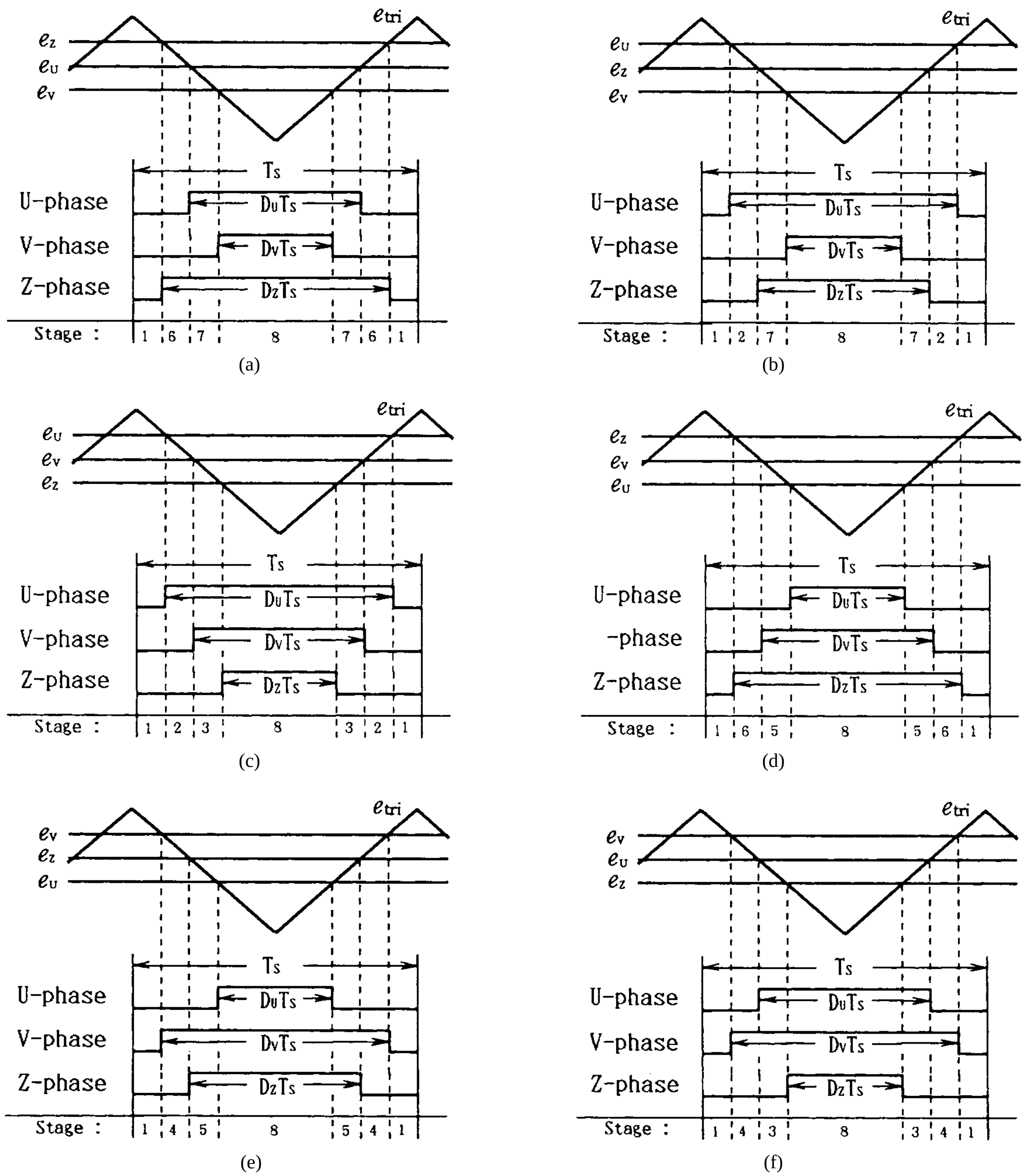

Fig. 5. Switching patterns for legs $U, V,$ and Z of rectifier

Since the switching frequency is very high compared to the ac input frequency and the parameters of the circuit components $(L, C,$ and $r)$ are selected to have very short time constants, the inductor currents and input capacitor voltages can be changed quickly. If stability of the control system is maintained, the ac inductor currents and the capacitor voltages are traced instantaneously to the control signal with little error. Therefore, we can analyze the system at each instant, as if the input voltage had a constant value. We classify the system characteristics of the above condition as the "the low-frequency characteristics."

On the other hand, in order to analyze system stability, we have to consider the transient characteristics over very short time periods. We classify these characteristics as the "the high-frequency characteristics."

A. Analysis of Low-Frequency Characteristics

If stability of the current control system is maintained, the low-frequency component of the input currents $\bar{i}_U$ and $\bar{i}_V$ corresponds to the input ac voltage $\overline{v}_{\rm ac}$. Over a very short period of time, input ac voltage $\overline{v}_{\rm ac}$, can be considered to be a constant dc voltage. Therefore, state-space averaged variable $\overline{\boldsymbol{X}}$ is

$$\frac{d\overline{\boldsymbol{X}}}{dt} = 0. \tag{24}$$

Substituting (24) into (23), we obtain

$$\overline{\boldsymbol{X}} = -\boldsymbol{A}^{-1}\boldsymbol{B}\boldsymbol{V}. \tag{25}$$

Solving (25), low-frequency components $\bar{i}_U$ and $\bar{i}_V$ are

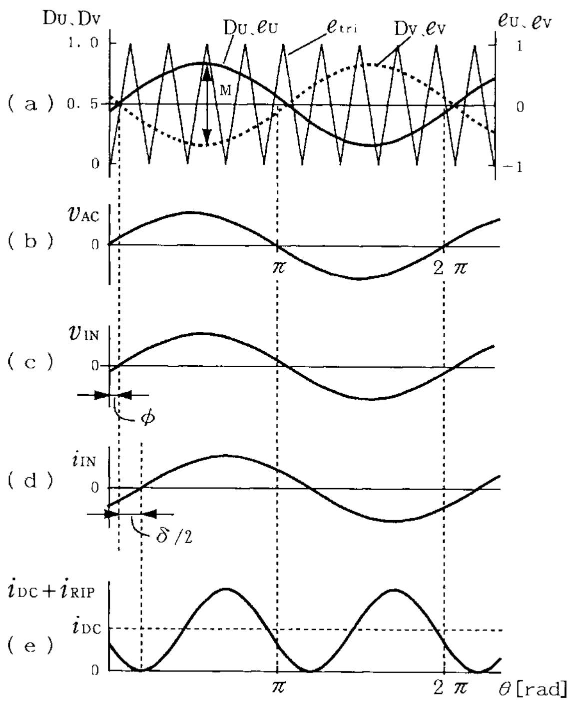

Fig. 6. Operation waveforms.

obtained as

$$\bar{i}_U = \frac{1}{2r}(-(D_U - D_V)\bar{v}_{\mathrm{dc}} + \bar{v}_{\mathrm{ac}}), \tag{26}$$

and

$$\bar{i}_V = \frac{1}{2r}((D_U - D_V)\bar{v}_{\mathrm{dc}} + \bar{v}_{\mathrm{ac}}). \tag{27}$$

Fig. 3 leads to

$$\bar{v}_{\mathrm{ac}} = r\bar{i}_U + \bar{v}_{UV} - r\bar{i}_V. \tag{28}$$

Substituting (26) and (27) into (28), the relationship between $\bar{v}_{UV}$ and $\bar{v}_{\mathrm{dc}}$ can be expressed as

$$\bar{v}_{\mathrm{UV}} = (D_U - D_V)\bar{v}_{\mathrm{dc}}. \tag{29}$$

Usually, voltages $r\bar{i}_U$ and $r\bar{i}_V$ are small compared to $\bar{v}_{\mathrm{ac}}$ and $\bar{v}_{UV}$, and $\bar{v}_{\mathrm{ac}}$ is approximated by

$$\bar{v}_{\mathrm{ac}} \cong \bar{v}_{UV} = (D_U - D_V)\bar{v}_{\mathrm{dc}}. \tag{30}$$

In the present PWM rectifier circuit, PWM with the unipolar voltage switching scheme [5] is applied. The modulation factor λ, which is the ratio between the control signal voltage and the modulation signal voltage e_{tri}, is defined as shown in Fig. 6. Therefore, the relationships between λ, D_U, and D_V can be expressed as

$$D_U = 0.5(1+\lambda) \tag{31}$$

$$D_V = 0.5(1-\lambda) \tag{32}$$

$$D_U + D_V = 1. \tag{33}$$

Since the ac input voltage has a sinusoidal waveform, the modulation factor λ is assumed to be a sinusoidal function written as

$$\lambda = \lambda_m \sin(\theta - \phi) \tag{34}$$

where λ_m is the peak-to-peak value of λ and ϕ is the phase angle between the λ zero crossing and the input voltage waveform (v_{ac}) zero crossing. Substituting (31)–(33) into (30), we obtain

$$\bar{v}_{\mathrm{ac}} \cong (D_U - D_V)\bar{v}_{\mathrm{dc}} = \lambda \bar{v}_{\mathrm{dc}}. \tag{35}$$

Notice that the dc output voltage $\bar{v}_{\mathrm{dc}}$ can be determined from both the input voltage $\bar{v}_{\mathrm{ac}}$ and the modulation factor λ, but is not influenced by the Z-phase duty ratio Dz. Consequently, the proposed PWM rectifier can be controlled to provide a sinusoidal input current waveform as though it were a conventional PWM rectifier.

B. Analysis of High-Frequency Characteristics

When a slight perturbation ΔD_m is applied to a given duty ratio D_m $(m = u, v,$ and $z)$, a slight fluctuation $\Delta\overline{\boldsymbol{X}}$, is seen in state variable $\overline{\boldsymbol{X}}$. Then, (23) is modified to represent small signal dynamic characteristic as

$$\frac{d\Delta\overline{\boldsymbol{X}}}{dt} = \boldsymbol{A}\Delta\overline{\boldsymbol{X}} + \frac{\partial \boldsymbol{B}}{\partial D_m}\boldsymbol{V}\Delta D_m \tag{36}$$

where

$$\Delta\overline{\boldsymbol{X}} = [\Delta\bar{i}_U \quad \Delta\bar{i}_V \quad \Delta\bar{v}_{C1}]^T.$$

By performing a Laplace transform on (36), $\Delta\overline{\boldsymbol{X}}(s)$ becomes

$$\Delta\overline{\boldsymbol{X}}(s) = (\boldsymbol{SI} - \boldsymbol{A})\boldsymbol{k}(s) \tag{37}$$

where

$$\boldsymbol{k}(s) = \frac{\partial \boldsymbol{B}}{\partial D_m}\boldsymbol{V}\Delta D_m(s).$$

Therefore, the transfer functions in terms of duty ratios $\Delta D_U, \Delta D_V, \Delta D_z$, respectively, are

$$\frac{\Delta\overline{\boldsymbol{X}}(s)}{\Delta D_U(s)} = \frac{-\bar{v}_{\mathrm{dc}}}{LP(s)}\begin{pmatrix} s\left(s+\dfrac{r}{L}\right)+\dfrac{1}{2LC} \\ -\dfrac{1}{2LC} \\ -\dfrac{1}{2C}\left(s+\dfrac{r}{L}\right)\end{pmatrix} \tag{38}$$

$$\frac{\Delta\overline{\boldsymbol{X}}(s)}{\Delta D_V(s)} = \frac{-\bar{v}_{\mathrm{dc}}}{LP(s)}\begin{pmatrix} -\dfrac{1}{2LC} \\ s\left(s+\dfrac{r}{L}\right)+\dfrac{1}{2LC} \\ -\dfrac{1}{2C}\left(s+\dfrac{r}{L}\right)\end{pmatrix} \tag{39}$$

and

$$\frac{\Delta\overline{\boldsymbol{X}}(s)}{\Delta D_Z(s)} = \frac{\bar{v}_{\mathrm{dc}}}{LP(s)}\begin{pmatrix} \dfrac{s}{L}\left(s+\dfrac{r}{L}\right) \\ \dfrac{s}{L}\left(s+\dfrac{r}{L}\right) \\ -\dfrac{1}{LC}\left(s+\dfrac{r}{L}\right)\end{pmatrix} \tag{40}$$

where

$$P(s) = s^3 + \frac{2r}{L}s^2 + \left(\frac{r^2}{L^2}+\frac{2}{LC}\right)s + \frac{r}{L^2C}.$$

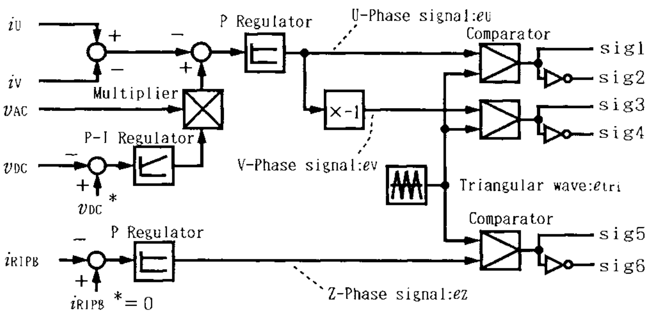

Fig. 7. Control block diagram of proposed PWM rectifier.

Using (38)–(40) and $\Delta D_U = -\Delta D_V$, the expressions for $\bar{i}_U(s)$ and $\bar{i}_V(s)$ in terms of $\Delta D_U, \Delta D_V$, and ΔD_Z are

$$\begin{aligned}\Delta\bar{i}_U(s) =& \frac{\partial\bar{i}_U(s)}{\partial D_U(s)}\Delta D_U(s) + \frac{\partial\bar{i}_U(s)}{\partial D_V(s)}\Delta D_V(s) \\ &+ \frac{\partial\bar{i}_U(s)}{\partial D_Z(s)}\Delta D_Z(s) \\ =& -\frac{\bar{v}_{\mathrm{dc}}}{L}\frac{1}{s+\frac{r}{L}}\Delta D_U(s) + \frac{\bar{v}_{\mathrm{dc}}}{L}\frac{1}{s^2+\frac{r}{L}s+\frac{1}{LC}} \\ &\cdot \Delta D_Z(s)\end{aligned} \tag{41}$$

and

$$\begin{aligned}\Delta\bar{i}_V(s) =& \frac{\partial\bar{i}_V(s)}{\partial D_U(s)}\Delta D_U(s) + \frac{\partial\bar{i}_V(s)}{\partial D_V(s)}\Delta D_V(s) \\ &+ \frac{\partial\bar{i}_V(s)}{\partial D_Z(s)}\Delta D_Z(s) \\ =& -\frac{\bar{v}_{\mathrm{dc}}}{L}\frac{1}{s+\frac{r}{L}}\Delta D_V(s) + \frac{\bar{v}_{\mathrm{dc}}}{L}\frac{1}{s^2+\frac{r}{L}s+\frac{1}{LC}} \\ &\cdot \Delta D_Z(s).\end{aligned} \tag{42}$$

Consequently, the transfer functions of the input current $\bar{i}_V(s)$ and Z-phase current $\bar{i}_z(s)$ are obtained as

$$\frac{\Delta\bar{i}_{\mathrm{IN}}(s)}{\Delta D_U(s)} = \frac{\Delta\bar{i}_U(s) - \Delta\bar{i}_V(s)}{2\Delta D_U(s)} = -\frac{\bar{v}_{\mathrm{dc}}}{2L}\frac{1}{s+\frac{r}{L}} \tag{43}$$

and

$$\frac{\Delta\bar{i}_Z(s)}{\Delta D_Z(s)} = \frac{\Delta\bar{i}_U(s) + \Delta\bar{i}_V(s)}{\Delta D_Z(s)} = \frac{2\bar{v}_{\mathrm{dc}}}{L}\frac{1}{s^2+\frac{r}{L}s+\frac{1}{LC}}. \tag{44}$$

On the basis of transfer function (43), the control block diagram of current i_{IN} can be represented as shown in Fig. 8(a). In this figure, the P regulator is used as the current regulator. Fig. 8(b) shows the transient response to a step change in the reference current, i^*_{IN}. Experimental results coincide well with the theoretical values. If the current i_{IN} follows its reference within a range of tenths of microseconds, then i_{IN} can be controlled to the reference signal, which changes according to the input ac (50/60 Hz) waveform.

Output dc current $\bar{i}_{\mathrm{OUT}}$ is calculated in the same way as $\bar{i}_U$ and $\bar{i}_V$, using the state-space averaging method. For example, mode (a) in Fig. 5 is calculated as follows:

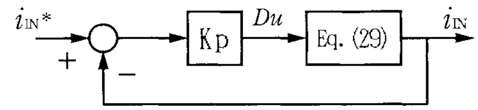

(a)

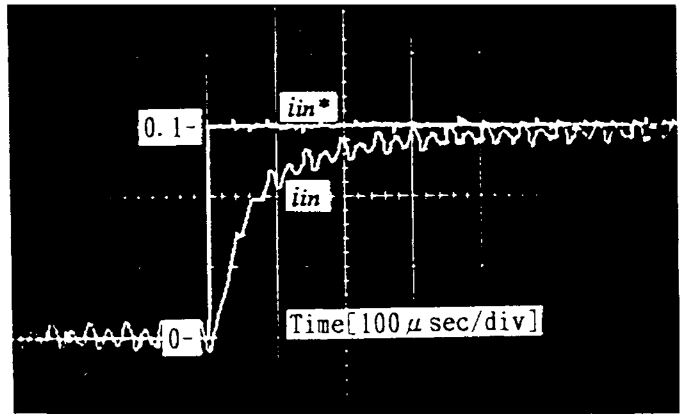

(b)

Fig. 8. A portion of control block diagram of current i_{IN} and transient response of i_{IN}.

stage (1) and (8)—the duty ratio is $D_1 = D_V + (1 - D_Z)$ and the output current is $\bar{i}_{\mathrm{OUT1}} = 0$;

stage (7)—the duty ratio is $D_2 = D_U - D_V$ and the output current is $\bar{i}_{\mathrm{OUT2}} = -\bar{i}_V$;

stage (6)—the duty ratio is $D_3 = D_Z - D_U$ and the output current is $\bar{i}_{\mathrm{OUT3}} = -(\bar{i}_U + \bar{i}_V)$.

The averaged output current $\bar{i}_{\mathrm{OUT}}$ is represented in (45), and the same result is obtained for the other modes, (b)–(f):

$$\begin{aligned}\bar{i}_{\mathrm{OUT}} &= D_1 \cdot \bar{i}_{\mathrm{OUT1}} + D_2 \cdot \bar{i}_{\mathrm{OUT2}} + D_3 \cdot \bar{i}_{\mathrm{OUT3}} \\ &= (D_U - D_Z)\bar{i}_U + (D_V - D_Z)\bar{i}_V.\end{aligned} \tag{45}$$

Substituting the input current $\bar{i}_{\mathrm{IN}} = 1/\sqrt{2}I_{\mathrm{IN}} \cdot \sin(\theta - \phi - \delta)$ and (31), (32), and (34) into (45), $\bar{i}_{\mathrm{OUT}}$ is expressed as

$$\begin{aligned}\bar{i}_{\mathrm{OUT}} =& \left(\frac{1}{2} - D_Z\right)\bar{i}_Z - \frac{\lambda}{\sqrt{2}}I_{\mathrm{IN}}\cos(2\theta - 2\phi - \delta) \\ &+ \frac{\lambda}{\sqrt{2}}I_{\mathrm{IN}}\cos\delta.\end{aligned} \tag{46}$$

It is clear that $\bar{i}_{\mathrm{OUT}}$ contains a dc current component $\bar{i}_{\mathrm{dc}}$ and a ripple component $\bar{i}_{\mathrm{RIP}B} = \bar{i}_{Z\mathrm{dc}} + \bar{i}_{\mathrm{RIP}}$. Reduction of the ripple current on the dc line is performed by maintaining $\bar{i}_{\mathrm{RIP}B} = 0$:

$$\bar{i}_{Z\mathrm{dc}} = \left(\frac{1}{2} - D_Z\right)\bar{i}_Z \tag{47}$$

$$\bar{i}_{\mathrm{RIP}} = -\frac{\lambda}{\sqrt{2}}I_{\mathrm{IN}}\cos(2\theta - 2\phi - \delta) \tag{48}$$

$$\bar{i}_{\mathrm{dc}} = \frac{\lambda}{\sqrt{2}}I_{\mathrm{IN}}\cos\delta. \tag{49}$$

Consequently, the current control block diagram for reducing ripple current is structured as shown in Fig. 9(a). In Fig. 9(a), i_{RIP} is disturbance in the feedback control of $i_{\mathrm{RIP}B}$. Fig. 9(b) shows the amount of disturbance suppression $(i_{\mathrm{RIP}B}/i_{\mathrm{RIP}})$. This figure shows that, at 100 Hz, the ripple

TABLE I
TEST CONDITIONS AND CIRCUIT PARAMETERS

Test Conditions			Circuit Parameters	
Input AC Voltage	v_{AC}	50V(peak)	AC Inductor L1, L2	480μH
Input AC Power	PAC	100W	Resistive Component of L1, L2	0.1Ω
Input Frequency	FAC	50Hz	AC Capacitor C1, C2	165μF
Input Power Factor		1.0	Output DC Capacitor	1200μF
Output DC Voltage	v_{DC}	140V	Switching Device S1～S6	IGBT
Switching Frequency	FS=1/TS	20kHz	(600V/75A, Type:2MBI75J-060, Fuji Electric)	
Mudulatin Factor	λ	0.36	Battery B1	12V-6AH×12 Series
Output Ripple Frequency		100Hz	(Type:12m-2, Furukawa Battery)	

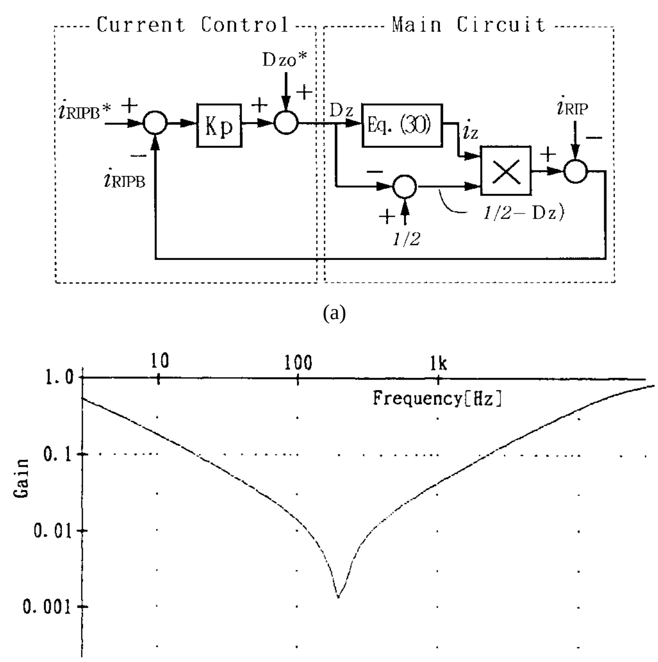

(a)

(b)

Fig. 9. A portion of control block diagram of current i_{RIPB} and characteristics of disturbance suppression.

current i_{RIPB} is suppressed to $1/100$ of its magnitude, and the ripple current i_{RIP} is converted to Z-phase current.

As discussed previously, a very simple control strategy can be applied. In the control block diagram shown in Fig. 7, sig1–sig6 represent the trigger signals of the main switches $S1$–$S6$, respectively. For input current control, the current reference i_{IN}^* is obtained by multiplying the input voltage waveform signal v_{ac} and the output of the dc voltage regulator. The input ac current i_{IN} is obtained from calculation block $\{(i_U - i_V)/2\}$. Since one of the inputs to the error amplifier $Kp1$ is i_{IN} and the other is i_{IN}^*, the output of the error amplifier is the control signal e_U. The control signal e_V is obtained by multiplying e_U by -1. Control signals e_U and e_V are modulated at the comparators by the triangular waveform e_{tri}. The output of the comparators are the triggering signals sig1–sig4. For ripple compensation control, the ripple current i_{RIPB} and the reference signal i_{RIPB}^* are the inputs to the error amplifier $Kp2$. The output is the control signal e_Z. The control signal e_Z is modulated by e_m, mentioned previously.

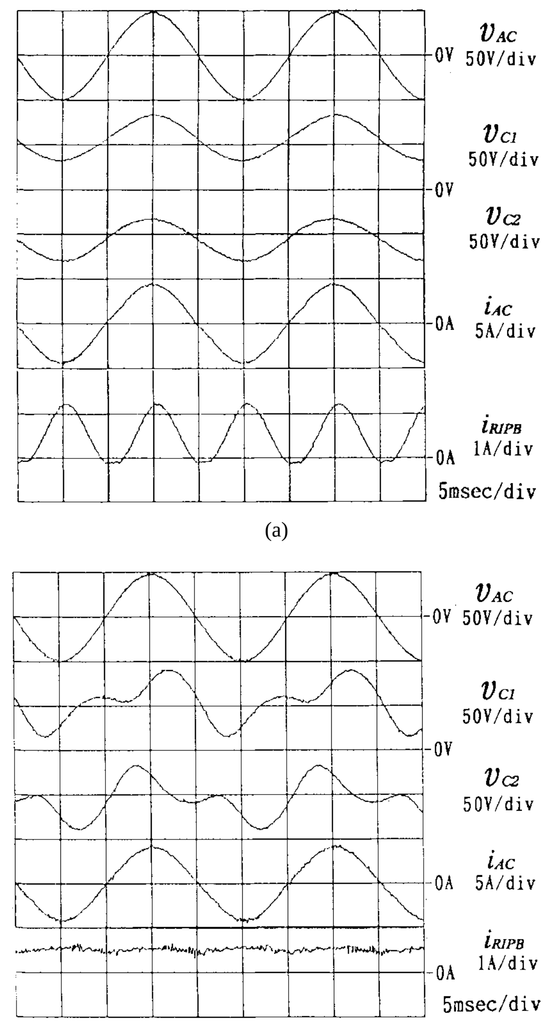

(a)

(b)

Fig. 10. Experimental waveforms. (a) Without compensation circuit. (b) With compensation circuit.

In the following experiment, values $Kp1$ $(Kp = 10)$ and $Kp2$ $(Kp2 = 10)$ are selected for maximum stability. An analysis of the optimum regulator gain will be discussed in another paper.

V. EXPERIMENTAL RESULTS

The parameters and conditions of the experimental PWM rectifier are shown in Table I. DC output capacitor Cd is used only for reducing the high-frequency switching ripple current. Therefore, it does not reduce the ripple current caused by input power rectification. Fig. 10(a) and (b) shows the operating waveforms of the rectifier with a sinusoidal ac input voltage. As shown in both figures, input current $i_{\rm ac}$ maintains a sinusoidal waveform. The dc ripple current $i_{{\rm RIP}B}$ of Fig. 10(b) is suppressed much more than the current $i_{{\rm RIP}B}$ shown in Fig. 10(a). The RMS value of the reduced ripple current is about $1/10$ of the noncompensated value. The capacitor voltage, labeled v_{C1} and v_{C2} in Fig. 10(b), are very distorted, whereas the input ac voltage has a sinusoidal waveform. The presence of distortion indicates the operation of ripple energy compensation, as calculated in (9)–(11). Since voltage waveform distortion is limited by circuit conditions such as $v_{\rm dc}, v_{\rm ac}$, and λ, the capacitance of C_1 and C_2 must be high in order to obtain high compensation. Because high capacitance causes a lead-phase input current, the capacitance should be set to the minimum values at which the ripple energy can be handled.

VI. Conclusions

In this paper, a novel circuit topology for a PWM rectifier was proposed. The proposed PWM converter is designed to produce both unity power factor with a sinusoidal input current and to reduce the dc ripple current flowing into an output-side battery. The unique features of this circuit topology are the Z-phase switches connected to the dc line and series-connected ac capacitors. The operating principle, a theoretical analysis, the control scheme, and experimental data on the proposed rectifier were presented. The ripple current flowing into a battery is significantly reduced by control of the Z-phase switches. Analytical equations were obtained using the state-space averaging method, and the transfer functions for ac input current control and for dc ripple compensation at both low and high frequency were presented. The experimental results coincide well with the theoretical values and show that the dc ripple current is reduced to approximately $1/10$ that of the conventional PWM rectifiers. This circuit topology is advantageous for applications requiring dc ripple current reduction, such as UPS's and dc power supplies.

References

[1] K. Toyama, T. Takeshita, and N. Matsui, "An approach to a reduction of a DC voltage ripple of a single-phase PWM converter," in *Proc. 1993 Nat. Conv. IEEJ-IAS*, p. 273.

[2] H. Irie, T. Yamashita, and N. Takemoto, "Ripple compensation for a single-phase rectifier by 2-quadrant chopper and auxiliary capacitor," *Trans. Inst. Electr. Eng. Jpn. D*, vol. 112-D, no. 7, pp. 623–629, July 1992.

[3] T. Shimizu, T. Fujita, G. Kimura, and J. Hirose, "Unity-power-factor PWM rectifier with DC ripple compensation," *Trans. Inst. Electr. Eng. Jpn. D*, vol. 114-D, no. 12, pp. 1298–1299, Dec. 1994.

[4] K. Harada, T. Ninomiya, and B. Gu, *The Fundamentals of Switched-Mode Converters.* Tokyo, Japan: Corona, 1992, pp. 41–46.

[5] N. Mohan, T. M. Underland, and W. P. Robbins, *Power Electronics: Converters, Applications, and Design.* New York: Wiley, 1989, pp. 119–122.

[6] C. Chen and D. M. Divan, "Simple topologies for single-phase AC line conditioning," in *Proc. IEEE-IAS Annu. Meeting*, 1991, pp. 911–917.

Toshihisa Shimizu (M'93) was born in Tokyo, Japan, in 1955. He received the B.S., M.S., and Ph.D. degrees in electrical engineering from Tokyo Metropolitan University, Tokyo, Japan, in 1978, 1980, and 1991, respectively.

He joined Fuji Electric Corporate Research and Development, Ltd. in 1980. Since 1994, he has been with the Department of Electrical Engineering, Tokyo Metropolitan University, as an Associate Professor. His research interests include power converters, high-frequency inverters, photovoltaic power generation, UPS's, and EMI problems.

Dr. Shimizu is a member of the Institute of Electrical Engineers of Japan (IEEJ) and the Japan Society of Power Electronics.

Tsutomu Fujita was born in Tokyo, Japan, in 1963. He received the B.S. and M.S. degrees from Tokyo Metropolitan University, Tokyo, Japan, in 1994 and 1996, respectively.

He joined the East Japan Railway Company, Ltd., Tokyo, Japan, in 1996.

Mr. Fujita is a member of the Institute of Electrical Engineers of Japan (IEEJ).

Gunji Kimura (M'90) was born in Tokyo, Japan, in 1942. He received the B.S. and Ph.D. degrees in electrical engineering from Tokyo Metropolitan University, Tokyo, Japan, in 1966 and 1980, respectively.

He joined the Department of Electrical Engineering, Tokyo Metropolitan University, in 1966 as a Research Associate. He has been a Professor since 1994. His research interests include power converters, motor drives, and photovoltaic power generation.

Dr. Kimura is a member of the Institute of Electrical Engineers of Japan (IEEJ) and the Japan Society of Power Electronics.

Jun Hirose was born in Gunma, Japan, in 1966. He received the B.S. degree in electrical engineering from Yokohama National University, Yokohama, Japan, in 1988.

He joined Fuji Electric Company, Ltd., Tokyo, Japan, in 1988, where he is mainly engaged in the development and design of UPS's.